Influence of a random phase plate on the growth of the backward stimulated Brillouin scatter

C. Ruyer [*], A. Fusaro, A. Debayle, R. Capdessus, P. Loiseau, and P. E. Masson-Laborde

CEA, DAM, DIF, F-91297 Arpajon, France
and Université Paris-Saclay, CEA, Laboratoire Matière en Conditions Extrêmes, 91680 Bruyères-le-Châtel, France

We derive the analytical dispersion relation of a high-energy laser beam's backward stimulated Brillouin scattering (BSBS) in a hot plasma, that accounts both for the random phase plate (RPP) induced spatial shaping and its associated phase randomness. Indeed, phase plates are mandatory in large laser facilities where a precise control of the focal spot size is required. While the focal spot size is well controlled, such techniques produce small scale intensity variations that can trigger laser-plasma instabilities such as BSBS. Quantifying the resulting instability variability is shown to be crucial for understanding accurately the backscattering temporal and spatial growth as well as the asymptotic reflectivity. Our model, validated by means of a large number of three-dimensional paraxial simulations and experimental data, offers three quantitative predictions. The first one addresses the temporal exponential growth of the reflectivity by deriving and solving the BSBS RPP dispersion relation. A large statistical variability of the temporal growth rate is shown to be directly related to the phase plate randomness. Then, we predict the portion of the beam's section that is absolutely unstable, thus helping to precisely assess the validity of the vastly used convective analysis. Finally, a simple analytical correction to the plane wave spatial gain is extracted from our theory giving a practical and effective asymptotic reflectivity prediction that includes the impact of phase plates smoothing techniques. Hence, our study sheds light on the long-time studied BSBS, deleterious to many high-energy experimental studies related to the physics of inertial confinement fusion.

I. INTRODUCTION

Advances in laser science offer opportunities for creating unprecedented energy density levels, via high-energy experiments on laser facilities such as the Laser Mégajoule (LMJ) [1,2], the National Ignition Facility (NIF) [3,4], and the SG-III [5,6], allowing to bring matter under extreme conditions, in particular relevant for laboratory astrophysics [7], high-energy density physics [8], or ignition purpose. The strong interplay between the laser electromagnetic pulse and the collective dynamics of the particles and fields of the plasma triggers a number of wave particle and wave mixing processes, which can give rise to new physical effects such as anomalous plasma heating [9], fast particle generation [10], significant backscattering [11–13], beam pointing direction deviation [14,15], and subsequent energy deposition [16,17]. Unfortunately, these processes are not independent from each other and can occur concurrently and lead to nonlinear effects, adding to the complexity of physics of laser created plasmas.

In order to improve the control on the pulse propagation, most high-energy laser facilities use so-called smoothing techniques such as random phase plates (RPP), spectral dispersion (SSD), or polarization smoothing (PS) which result in degrading the spatial, temporal, or polarization laser coherence, respectively [18,19]. The produced intensity profile

is composed of microns-scale fluctuations resulting from the spatial multimode pattern interferences, the so-called speckles (or hot spots) which vanish and change position periodically if SSD is used [20–22]. Many experimental and theoretical studies demonstrate that degrading the laser coherence indeed improves the laser propagation [23–26], albeit without completely stabilizing most wave mixing processes as notably cross beam energy transfer [27–30] or stimulated Raman backscattering [31–33], which have been characterized in these conditions. Hence, the groundwork and predictions associated with these experiments are further complicated due to the entanglement between the laser plasma instabilities and the pump wave controlled incoherence.

In this context, it is convenient to use a linear convective gain analysis [34] using plasma conditions given by a radiative-hydrodynamic code. This approach is based on a crude plane wave convective gain which can be embedded in the ray tracing scheme [35,36] used for modeling the laser propagation, giving a first estimate of the deleterious laser-plasma effects. However, these tools still fail to predict a stimulated Brillouin scattering (BSBS) reflectivity because of their inherent simplifying assumptions. The bypass of this difficulty motivated nonpredictive analysis, such as the feeding of measured experimental reflectivity levels for correcting the laser pulse used in post-shot simulations, thus modifying the convective gain analysis [35], but helping to interpret experiments. An improvement of the laser propagation modeling is to use, in addition to radiative-hydrodynamics numerical results, large scale paraxial simulations [37] which take

---

[*]charles.ruyer@cea.fr

035208-1

naturally into account the laser incoherence and particularly the phase plate induced speckles.

Pinpointing the speckles contribution to the whole beam backscattering level has essentially been done through the use of their known intensity distribution. In this case, speckles are randomly distributed over the focal volume, with an intensity reaching up to 10 times the mean laser intensity with known correlation lengths and intensity probability distribution in vacuum. This intensity distribution may be used to calculate averaged quantities in the limit where each speckle is spatially independent of the other and has led to numerous interesting BSBS models [38–40]. However, this either locates the acoustic fluctuations to the speckle vicinity [41–43] or oppositely assumes that their propagation spans many hot spots [44], therefore putting a strong constraint on the acoustic damping rate. Indeed, dealing directly with the phase randomness constitutes a major difficulty, that has been either neglected [45] or averaged out [46,47].

In this article, we stand out from such assumptions and propose a formalism, based on accurate analytical modeling, which accounts for the influence of the randomness of the phase plate on the spatial and temporal BSBS growth rate. In doing so, we can quantitatively predict the reflectivity of a realistic laser beam. A comparison with a large number of three-dimensional (3D) hydrodynamic paraxial Hera [48,49] simulations validates our predictions and demonstrates that accounting for the phase plate randomness is crucial for understanding the impact of the phase plates on the temporal and convective BSBS amplification [50].

The layout of the paper is organized as follows: We first derive the BSBS RPP dispersion relation in Sec. II and extract a solution which is relevant to the reflectivity temporal growth, as addressed in Sec. III. The absolute stability condition is also derived and discussed in light of a comparison with an independent-speckle model. We then address the BSBS asymptotic regime described in Sec. IV by a convective amplification and apply our analytical model to predict the RPP spatial BSBS gain. In Sec. V, we derive a correcting multiplying factor to the convective plane wave gain which allows to evaluate the RPP beam asymptotic reflectivity. We finally confront our model to ICF-relevant backscattering measurements. Note that throughout this paper, the SI unit system will be used while dropping the Boltzmann constant and noting the vectors in bold symbols.

II. GENERAL RPP BSBS DISPERSION RELATION

A. Derivation of the dispersion relation

The linearized density fluctuations $\delta n_e/n_e$ may be related to the perturbed scattered amplitude δE in the Fourier space $(\omega_s, \mathbf{k}_s)$ and the pump field E_p. We now introduce ϵ_0, n_c, c_s, $\nu_s = |\mathbf{k}_s|\bar{\nu}c_s$, $n_{e/i}$, $Z_{e/i}$, $T_{e/i}$, $m_{e/i}$, the permittivity of vacuum, the laser critical density, the sound speed, the Landau acoustic damping rate, the electron/ion density, charge number, temperature, and mass, respectively. The usual procedure derived in an infinite and homogeneous plasma at rest is followed [51], perturbing the electron density and the velocity, $n = n_e + \delta n_e$ and $\mathbf{v}_e = 0 + \delta\mathbf{v}_e$, respectively. We neglect the electron inertia and assume the electron pressure evolution to be isothermal.

For adiabatic ions of index $\gamma_i = 3$, the conservation of density and momentum verifies (to leading order in δn_e and $\delta\mathbf{v}_e$)

$$\frac{\partial_t \delta n_e}{n_e} = -\boldsymbol{\nabla}\delta\mathbf{v}_e, \tag{1}$$

$$\partial_t \delta\mathbf{v} + 2\nu_s \delta\mathbf{v} = -c_s^2 \boldsymbol{\nabla}\frac{\delta n_e}{n_e} - \frac{Z_i \epsilon_0}{2 m_i n_c}\boldsymbol{\nabla}E_p \delta E. \tag{2}$$

The combination of these equations leads to

$$\left[c_s^2 \nabla^2 - \partial_t \partial_t - 2\nu_s \partial_t\right]\frac{\delta n_e}{n_e} = -\frac{Z_i \epsilon_0}{2 m_i n_c}\nabla^2 E_p \delta E. \tag{3}$$

Performing a Fourier transform, defined as $\hat{f} = \int f e^{-i\mathbf{k}\cdot\mathbf{r}+i\omega t}d\mathbf{r}\,dt$, we obtain [52]

$$\frac{\delta n_e}{n_e}(\omega_s, \mathbf{k}_s) = -\alpha_f(v_\phi)\frac{\epsilon_0 E_p}{2 n_c T_e}\otimes\delta E^\star, \tag{4}$$

$$\alpha_f = \kappa\frac{\bar{c}_s^2}{\bar{c}_s^2 - v_\phi^2 - 2i\bar{\nu}v_\phi\bar{c}_s},$$

$$\bar{c}_s^2 = \frac{Z_i T_e/g^2 + 3T_i}{m_i}, \tag{5}$$

while $v_\phi = \omega_s/|\mathbf{k}_s|$, $\kappa = Z_i T_e/m_i c_s^2$, $g = \sqrt{1 + \mathbf{k}_s^2\lambda_{De}^2}$, with $\lambda_{D,e/i}$ the electron/ion Debye length and $u^\star$ the complex conjugate of u. We have also introduced the convolution product in the Fourier space $\otimes$. Note that along Eq. (5), $c_s = \sqrt{(Z_i T_e + 3T_i)/m_i}$ corresponds to the low wave vector limit of the acoustic phase speed. The factor g in Eq. (5) does not directly derive from the above fluid formalism but from a Taylor development of the kinetic equations [Eqs. (6) and (7)]. As our predictions will be confronted with a hydrodynamic code, the fluid plasma response will be considered except in Sec. V C where a multi-ion species plasma requires the use of a kinetic formalism. Reference [53] presents a plasma density response to the beating of a pump and a scattered electromagnetic wave that derives from the linearization of the Vlasov equation. A formula similar to Eq. (4) is obtained while replacing α_f by α_k, i.e.,

$$\alpha_k = \mathbf{k}_s^2\lambda_{D,e}^2\frac{\chi_e\left(1 + \sum_i \chi_i\right)}{1 + \chi_e + \sum_i \chi_i}, \tag{6}$$

$$\chi_{e/i} = \frac{-1}{2\mathbf{k}_s^2\lambda_{D,e/i}^2}\mathcal{Z}'(v_\phi\sqrt{m_{e/i}/2T_{e/i}}), \tag{7}$$

while $\mathcal{Z}'$ is the first order derivative of the plasma dispersion function [54]. In the kinetic formalism, the sound speed will be related to the phase speed value that maximizes the imaginary part of Eq. (6), $v_\phi^{max} = \bar{c}_s \simeq c_s/g$. For a linear polarization, the associated scalar electric field has been modeled, in a three-dimensional (3D) system in Refs. [55–57], and is valid only at the focal plane. We will instead use the fields as introduced in Ref. [58] [Eq. (46)] which are valid slightly off focus such that

$$E_p(x, \mathbf{r}_\perp, t) = \frac{E_0}{N}e^{ik_0 x - i\omega_0 t}\sum_{\mathbf{k}}e^{i\Theta}e^{-i\frac{\mathbf{k}^2}{2k_0}(x - x_f)}, \tag{8}$$

$$\Theta = \mathbf{k}_\perp(\mathbf{n})\cdot\mathbf{r} + \phi_{\mathbf{k}}, \tag{9}$$

$$\mathbf{k} = k_y\hat{\mathbf{y}} + k_z\hat{\mathbf{z}} = \mathbf{n}2k_m/N, \tag{10}$$

$$\mathbf{n} = n_y\hat{\mathbf{y}} + n_z\hat{\mathbf{z}}, \tag{11}$$

where $n_{y/z}$ are unsigned integer and $N = \sum_{\mathbf{k}(\mathbf{n})} H[k_m^2 - \mathbf{k}(\mathbf{n})^2]$ is the number of phase plate elements. $H(x)$ designates the Heaviside function. The dependence on $\mathbf{n}$ of $\mathbf{k}$ will be dropped for simplicity. The unity vectors in the directions x, y, and z are noted $\hat{\mathbf{x}}$, $\hat{\mathbf{y}}$, and $\hat{\mathbf{z}}$, respectively. Hence, the sum in Eq. (8) runs over k_y and k_z, i.e., in a realistic geometry $|\mathbf{k}| = (k_y^2 + k_z^2)^{1/2} \leqslant k_m$ where $k_m = k_0/2f_\sharp$ with $k_0 = 2\pi/\lambda_0$ the main laser wave vector and $f_\sharp$ the optic f number. The last exponential of Eq. (8) accounts for diffraction to second order in $|\mathbf{k}|/k_0$ and includes x_f, the x position of the focal plane. Without this term, the speckles are infinite in the x direction, otherwise they have the expected length of $\sim \pi f_\sharp^2 \lambda_0$. The phases $\phi_\mathbf{k}$ are independent random variables taking the values 0 or π with equal probability. Under these conditions, and for $\langle w \rangle$ being the statistical average of the random variable w, we note that [59]

$$\langle e^{i\phi_{\mathbf{k}_1} - i\phi_{\mathbf{k}_2}} \rangle = \delta_{\mathbf{k}_1, \mathbf{k}_2}. \tag{12}$$

Here $\delta_{\mathbf{k}_1, \mathbf{k}_2}$ designates the Kronecker symbol. It is extremely tempting to simplify the wave mixing equations by using formula (12) which has led to interesting results [45,46]. Instead, we will carefully carry the calculations while keeping the phase plate randomness. This is indeed of crucial importance to quantitatively understand the BSBS of a smoothed beam, as shown subsequently.

As shown in Refs. [21,59], the pump field above consistently captures the expected speckle properties such as their intensity distribution or coherence length.

We now introduce

$$\mathbf{k}_{0,1} = (k_0 - \mathbf{k}_1^2/2k_0)\hat{\mathbf{x}} + \mathbf{k}_1, \tag{13}$$

$$\mathbf{k}_{0,2} = (k_0 - \mathbf{k}_2^2/2k_0)\hat{\mathbf{x}} + \mathbf{k}_2, \tag{14}$$

$$D_-(\mathbf{k}_{0,1}) = (\omega_s - \omega_0)^2 - \omega_{pe}^2 - (\mathbf{k}_s - \mathbf{k}_{0,1})^2 c^2, \tag{15}$$

where ω_{pe} is the electron plasma frequency, ω_s is the frequency of the acoustic wave. Note that Eqs. (13) and (14) verify $|\mathbf{k}_1| = |\mathbf{k}_2| = k_0$ to second order in $|\mathbf{k}_1|/k_0$ and $|\mathbf{k}_2|/k_0$. The derivation of the RPP dispersion relation detailed in Appendix A remains similar to Ref. [47] with the addition of a diffraction term and starts with the fields of Eq. (8), written in the Fourier space $(\omega_p, \mathbf{k}_p)$ and enveloped in space and time around $(\omega_0, k_0\hat{\mathbf{x}})$. When seeking for the backscattering growth in the vicinity of the focal spot, we shall apply $x_f = 0$ in the rest of the paper. We may also search for monochromatic growth of the acoustic fluctuations due to the linear approximation, so that

$$\delta n_e(\omega, \mathbf{k}) \propto \delta(\omega - \omega_s)\delta(\mathbf{k} - \mathbf{k}_s), \tag{16}$$

where $\delta(x)$ is the Dirac function. Such an approximation might seem too restrictive to treat the scattered growth driven by a nonhomogeneous pump wave. However, the direct relationship between the resulting growth rate probability distribution and spatial distribution, as done in Sec. II B, will justify the formalism used here. Hence, combining Eqs. (16) with (A5) and after integration over frequency and wave vectors, we obtain

$$1 = -\frac{n_e}{n_c}\left(\frac{v_{\mathrm{os}}}{v_{\mathrm{the}}}\right)^2 \frac{\omega_0^2}{4N} \sum_{\mathbf{k}_1} \sum_{\mathbf{k}_2} \frac{e^{i\phi_{\mathbf{k}_1} - i\phi_{\mathbf{k}_2}}}{D_-(\mathbf{k}_{0,2})}$$

$$\times \alpha_{k/f}\left(\frac{\omega_s}{|\mathbf{k}_s + \mathbf{k}_{0,1} - \mathbf{k}_{0,2}|}\right), \tag{17}$$

where $(v_{\mathrm{os}}/v_{\mathrm{the}})^2 = \epsilon_0 E_0^2/n_c T_e N$. Note that Eq. (16a) of Ref. [53] is recovered for $N = 1$. For a particular RPP (i.e., a given set of $\phi_\mathbf{k}$), the paraxial and experimental BSBS growth is expected to be strongly nonhomogeneous due to the presence of the speckles. Hence, because of the monochromatic assumption made earlier, the physical relevance of Eq. (17) regarding a particular RPP is questionable, so that we cannot claim to predict the BSBS associated with a distinct RPP. However, as shown subsequently, the resolution of Eq. (17) for *all possible RPP*, i.e., for all possible spatial speckle configurations, gives access to the spatial information required to quantitatively understand the spatial distribution of the RPP BSBS growth. The proper mathematical demonstration of that ansatz is beyond the scope of this study. However, it will enable to understand the temporal and spatial dynamics of the BSBS of RPP beam obtained in our simulations (Secs. III and IV) and an experiment (Sec. V C).

At this stage, obtaining a numerical solution of the above equation might be challenging due to the discrete sums that run over N^2 elements. However, analytical progress may be reached by simplifying the imaginary part of the plasma response function $\alpha_f(v_\phi)$ whose resonance peak is centered in $v_\phi = c_s$ and of width $2\bar{\nu}c_s$. For $f_\sharp \gtrsim 6.5$, and for $\bar{\nu} \gtrsim 5 \times 10^{-3}$, the argument of α_f is always close enough to c_s, i.e.,

$$\alpha_{k/f}\left(\frac{\omega_s}{|\mathbf{k}_s + \mathbf{k}_{0,1} - \mathbf{k}_{0,2}|}\right) \simeq \alpha_{k/f}\left(\frac{\omega_s}{|\mathbf{k}_s|}\right). \tag{18}$$

We thus have

$$1 = -\alpha_{k/f}(v_\phi)\frac{n_e}{n_c}\left(\frac{v_{\mathrm{os}}}{v_{\mathrm{the}}}\right)^2 \frac{\omega_0^2}{4N} \sum_{\mathbf{k}_1} \frac{S(\mathbf{k}_1)}{D_-(\mathbf{k}_{0,1})}, \tag{19}$$

$$S(\mathbf{k}_1) = \sum_{\mathbf{k}_2} e^{i\phi_{\mathbf{k}_1} - i\phi_{\mathbf{k}_2}}. \tag{20}$$

The phase plate randomness has been gathered in the variable S. Its variance verifies $\langle (S-1)^2 \rangle = N$ and its mean value satisfies $\langle S \rangle = 1$ [using Eq. (12)]. Equations (19) and (20) naturally include the interplay between the RPP beam and the plasma. In particular, the possible correlation effects between the randomly distributed hot spots and the acoustic waves are accounted for, whether the plasma is heavily Landau damped or not. We may now apply the central limit theorem and approximate S to the random normal law $\mathcal{N}(1, N)$ centered in unity and of variance N. Note that when replacing S by a normal law, we do keep the dispersion relation variability, unlike the direct combination of Eq. (19) with (12). The simplification of D_- may now be carried using $\omega_0^2 = \omega_{pe}^2 + k_0^2 c^2$ with $\omega_s^2 \ll \mathbf{k}_s^2 c^2$. We will also restrict, unlike Sec. IV, the following analysis to the x-axis backscattering, i.e., imposing $\mathbf{k}_s = k_s\hat{\mathbf{x}}$ and assuming that the BSBS of the RPP beam is correctly reproduced by the on-axis response

$$D_- \simeq D_0 - \frac{k_s}{k_0}\mathbf{k}_1^2 c^2 + O(|\mathbf{k}_1|^4/k_0^4),$$

$$D_0 = -\mathbf{k}_s^2 c^2 - 2(\omega_s\omega_0 - k_s k_0 c^2). \tag{21}$$

We therefore obtain

$$1 = -\frac{1}{4}\frac{n_e}{n_c}\left(\frac{v_{os}}{v_{the}}\right)^2 \omega_0^2 \alpha_{k/f}\left(\frac{\omega_s}{|k_s|}\right)\frac{\mathcal{N}(1,N)}{N}\sum_{\mathbf{k}_1}\frac{1}{D_0 - \frac{k_s}{k_0}\mathbf{k}_1^2 c^2}. \tag{22}$$

The above discrete sum runs over the many phase plate elements, and can be more easily calculated in the continuous limit. Assuming a cylindrical beam, the discrete sum in Eq. (22) may be replaced by a quadrature over $|\mathbf{k}_1| < k_m$ so that $N^{-1}\sum_{\mathbf{k}_1} \simeq \text{PV} \cdot \int_0^{k_m} dk_1 2\pi k_1/(\pi k_m^2)$ (where PV designates the principal value). Provided that the real part of D_0 fulfills $\text{Re}(D_0) \neq 0$,

$$D = 1 + \frac{1}{4}\frac{n_e}{n_c}\left(\frac{v_{os}}{v_{the}}\right)^2 \mathcal{N}(1,N)\alpha_{k/f}(v_\phi)\frac{\omega_0^2 k_0}{k_s k_m^2 c^2}$$

$$\times \ln\left(1 - \frac{k_m^2 c^2 k_s}{k_0 D_0}\right),$$

$$D = 0, \tag{23}$$

where ln is the principal value of the logarithm. The above dispersion relation accounts for the phase plate randomness and spatial incoherence and models how the temporal growth of the backscatter is affected.

In the plane wave limit, i.e., for infinite $f_\sharp$, the variance in the dispersion relation ($N \propto 1/f_\sharp^2$) vanishes and a Taylor development of the logarithm [or equivalently removing the sum in Eq. (22)] leads to the well known plane wave limit [53], from which an analytical solution exists.

As an example, the growth rate, obtained from the numerical resolution of $\langle D \rangle = 0$ [see Appendix B for the numerical solving of Eq. (23)] is illustrated as a dotted line in Fig. 1(a) and reaches the plane wave asymptotic limit when $f_\sharp \gtrsim 25$. Noticeably, it vanishes around $f_\sharp \simeq 9$ and drops to the free acoustic wave limit $\Gamma = -\nu_s = -0.0148\,\omega_s$, below [or $\Gamma = -0.1\omega_s$ for Fig. 1(b) when $f_\sharp \lesssim 21$]. Using the real scalar random variable $X \equiv \mathcal{N}(1,N)$, we may derive the threshold f number f_c, for which $D(\omega_s, k_s) = 0$. This leads to a purely real acoustic frequency (i.e., a vanishing growth rate). Noticing that at resonance, $\alpha_f(v_\phi = c_s/g)$ is a purely imaginary scalar, D may be purely real only if the logarithm in Eq. (23) has a purely imaginary value. Hence, setting the logarithm to $-i\pi$, we obtain

$$f_c = \eta/\sqrt{\pi X(n_e/n_c)(v_{os}/v_{the})^2(\kappa/4\bar{\nu})}, \tag{24}$$

where η is the optical index. For $X = 1$ and using the parameters of Figs. 1(a) and 1(b), we obtain $f_c \simeq 9$ and 21, respectively. This is in good agreement with the numerical values (see the value of $f_\sharp$ where the dotted line crosses $\Gamma = 0$). Likewise, the differentiation of Eq. (23) around $f_\sharp = f_c$ leads to the exact value of $d\Gamma/df_\sharp$ at $f_\sharp = f_c$,

$$\left.\frac{d\Gamma}{df_\sharp}\right|_{f_\sharp = f_c} = \text{Im}\left[\frac{2\alpha_f k_s}{f_c \alpha_f'}\left(\frac{2i}{\pi} - 1\right)\right], \tag{25}$$

where $\alpha_f'(v_\phi)$ is the derivative of $\alpha_f(v_\phi)$ versus v_ϕ. We propose to bridge the gap between $f_\sharp = f_c$ (where $\Gamma = 0$) and $f_\sharp \to \infty$ (where the plane wave value is reached, $\Gamma = \Gamma_{PW}$) by using a fitted hyperbolic tangent function
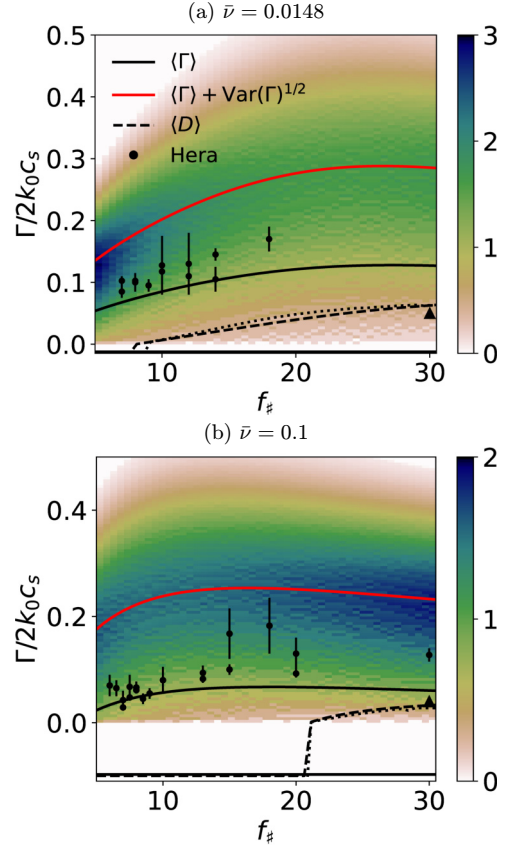

FIG. 1. (a), (b) The color map represents the probability distribution (normalized to $1/2k_0 c_s$) of the temporal growth rate, reconstructed with Eq. (27) and verifying $\int_{\Gamma \geqslant -\nu} p d\Gamma = 1$. The growth rate is given by Eq. (26). The numerical resolution of $\langle D \rangle = 0$ from Eq. (23) and the analytical approximate of Eq. (26) are superimposed as dotted and dashed lines, respectively. The solid black and solid red lines illustrate the dependence of $\langle \Gamma \rangle$ and $\text{Var}(\Gamma)^{1/2}$ on $f_\sharp$ (see legend). The growth rate extracted from the exponential growth of the reflectivity curve as predicted by three-dimensional Hera simulations is illustrated as black circles (see text) and 1D Hera results ($f_\sharp \to \infty$) are shown in black triangles placed at $f_\sharp = 30$. We consider a He^{2+} 10% critical plasma with a normalized acoustic Landau damping rate of $\bar{\nu} = 0.0148$ (a) and $\bar{\nu} = 0.1$ (b). Use has been made of $T_e = 2$ keV, $T_i = 1$ keV, $I_0 = 2 \times 10^{14}$ W/cm^2, $\lambda_0 = 0.35$ μm, and $N = L_y^2/(f_\sharp \lambda_0)^2$, $L_y = 200$ μm being the beam transverse size. The plasma response is here fluid [Eq. (5)].

such that

if $f_\sharp > f_c$,

$$\text{Im}(\omega_s) = \Gamma$$

$$= \Gamma_{PW}(XI_0)\tanh\left[\left(\frac{f_\sharp - f_c}{\Gamma_{PW}(XI_0)}\frac{d\Gamma}{df_\sharp}\Big|_{f_\sharp = f_c}\right)^{1/a}\right]^a,$$

otherwise,

$$\Gamma = -\bar{\nu}k_s c_s = -\nu_s, \tag{26}$$

with $k_s = 2k_0[1 - \omega_0/(k_0 c)(c_s/c)]$ and $a = (1/2) + (50/3)(\bar{\nu} - 0.01)$ and where $\Gamma_{PW}(XI_0)$ is the plane wave temporal growth rate [53] computed with a pump wave intensity of $I = XI_0$. The particular case $X = 1$ of the above
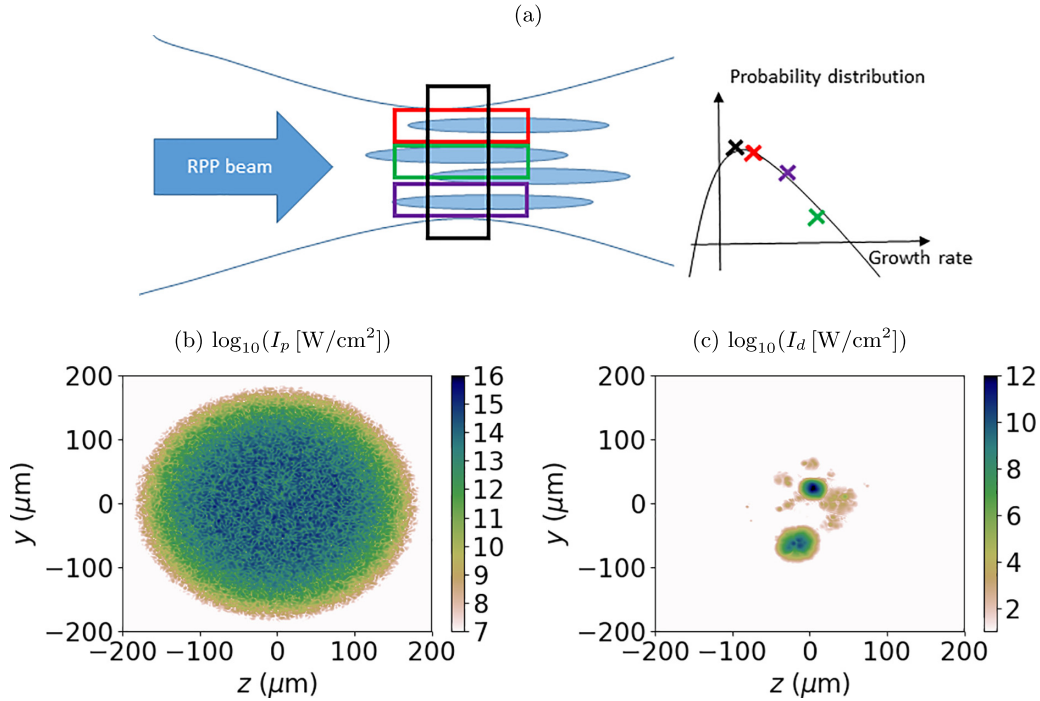
FIG. 2. (a) Sketch showing the relation between a probability distribution and a spatial distribution for a homogeneous and large enough RPP beam. Since the RPP elements are independent from each other, the growth rate probability distribution (right) may be sampled once over the whole beam (black box and cross) or similarly over large-enough subbeams (colored boxes and crosses). (b), (c) Intensity in logarithm scale of the pump and scattered wave as predicted by 3D Hera simulations [simulation detail in Sec. III A at $x = 0$ (the pump wave entry location)] . The plasma is composed of helium with $\bar{\nu} = 0.1$, $T_e = 2$ keV, $T_i = 1$ keV, $I_0 = 2 \times 10^{14}$ W/cm^2, $\lambda_0 = 0.35$ μm, and $f_\sharp = 10$.

solution is illustrated as a dashed line in Figs. 1(a) and 1(b) and demonstrates a good agreement with the numerical resolution (as dotted lines). The above fits local relative error fulfills <10% in the domain $0.01 \lesssim \bar{\nu} \lesssim 0.1$.

B. Probability and temporal growth rate spatial distribution

Since X is a random variable, the dependence on X of Eq. (26) implies that Γ is also a random variable. The BSBS temporal growth rate is therefore associated with a probability distribution that we propose now to reconstruct. As $X \equiv \mathcal{N}(1, N)$, the unstable solutions of Eq. (23) may be associated with the probability $\exp[-(X - 1)^2/2N]/\sqrt{2\pi N}$, thus leading to $\Gamma(X)$. Creating spatial growth rates bins such that $\Gamma_n = -\nu_s + n\,d\Gamma$ (where $d\Gamma$ is the bin step), we may sum the probability contribution of the events $\Gamma_n < \Gamma(X) < \Gamma_{n+1}$ to reconstruct numerically the discrete probability distribution

$$p(\Gamma_n) = \frac{dP}{d\Gamma}(\Gamma_n) = \sum_{\Gamma_n < \Gamma(X) < \Gamma_{n+1}} \frac{e^{-(X-1)^2/2N}}{\sqrt{2\pi N}} \frac{dX}{d\Gamma}. \quad (27)$$

Although $p(\Gamma)$ can be estimated analytically using the derivative of Eq. (26), we will settle subsequently with a numerical estimation. The convergence of $p(\Gamma_n)$, illustrated as a color map in Figs. 1(a) and 1(b) and 3(a) for a He^{2+} 10% critical plasma, is reached for a fine-enough discretization of the real variable X. In the following, the interval $[-3N^{1/2}, 3N^{1/2}]$ is split in 3000 regularly spaced bins. A first peak of the probability distribution is evidenced for $\Gamma = -\nu_s$, which corresponds to all the stable events as predicted by Eq. (26) [i.e.,

verifying $f_c(XI_0) > f_\sharp$]. All these stable contributions are gathered at the same value $\Gamma = -\nu_s$, leading to a Dirac-type shape. Hence, our numerical evaluation of p leads to the black feature (the color map is saturated there) in Figs. 1(a) and 1(b) located at $\Gamma = -\nu_s$. A second local maximum, around $\Gamma/2k_0c_s \sim 0.2$–0.3, corresponds to the most probable strictly positive growth rate and results from a tradeoff between the growth rate which is an increasing function of the random variable X and the associated probability that rapidly decreases.

Hence, Eqs. (22) and (23) give access to the growth rate probability distribution. As illustrated in Fig. 2(a), we may associate the various possible growth rates to different RPP realizations, thus identifying one statistical realization (black cross) to the whole beam (black box). However, the most interesting way to understand how the phase plate randomness affects the backscatter growth is to split the beam spatially. Since the phase plate elements are independent from each other, the large enough subparts of the beam [in colored boxes in Fig. 2(a)] correspond to independent samplings of the Γ random law (in colored crosses). Hence, the probability distribution as predicted by our dispersion relation is related to the portion of the beam which can be described by a given scalar growth rate. In other words, the growth rate probability distribution may be seen as a spatial distribution. As en example, the probability of having a strictly positive growth rate

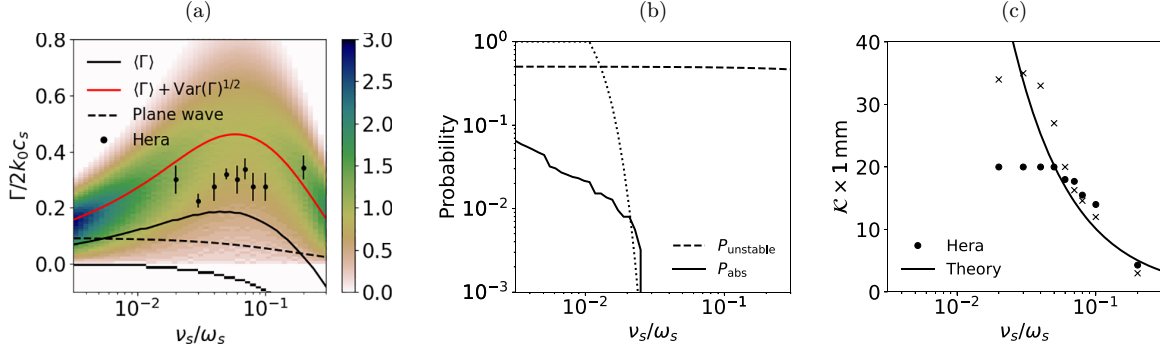$$P_{\text{unstable}} = \int_{\Gamma > 0} p\,d\Gamma \quad (28)$$

FIG. 3. (a) Growth rate normalized probability distribution, as a function of $\bar{v} = v_s/\mathrm{Re}(\omega_s)$. (b) Probability as predicted by Eqs. (28) (black dashed line) and (30) (black plain line). P_{abs} based on an independent speckle model [60,61] is superimposed as a black dotted line (see text). (c) Hera spatial gain, extracted from 3D RPP (circle) and 1D (crosses) Hera simulations by averaging $d_x \log(\langle I_d\rangle_y)$ over the first 200 μm of the simulations domain. The convective plane wave theory corresponds to the average of Eq. (38) (plain line). We consider a He^{2+} 10% critical plasma with $T_e = 3$ keV, $T_i = 1$ keV, $I_0 = 4 \times 10^{14}$ W/cm^2, $\lambda_0 = 0.35$ μm, and $N = L_y/(f_\sharp \lambda_0)$ with $f_\sharp = 8$, $L_y = 400$ μm. The plasma response is here fluid, Eq. (5).

corresponds to the portion of the beam which is really unstable and is here ∼50%. As expected, the scattered intensity of Fig. 2(d) [at $x = 0$, for the plasma parameters of Fig. 1(b), simulation details in Sec. III A] presents a significantly smaller section than the pump [in Fig. 2(c)]. Quantitatively, the section of Fig. 2(c) that is above noise level (here ∼4×10^{-2} W/cm^2) is indeed half the surface of the pump beam that fulfills $I_p \gtrsim 10^{14}$ W/cm^2, as predicted by our theory.

The statistical averaged growth rate $\langle\Gamma\rangle = \int_{\Gamma \geqslant -v_s} \Gamma p \, d\Gamma$ [as black plain lines in Figs. 1(a) and 1(b)] is as shown subsequently, the most relevant growth rate when compared to numerical results. Moreover, it is located significantly below the local maximum of the probability distribution due to the fact that roughly only half the beam is really unstable. The plane wave case [53] corresponds to the limit $f_\sharp \to \infty$ and is reached asymptotically by the solution of $\langle D\rangle = 0$ (as dashed black lines) and confirmed by 1D Hera simulations as a large triangle (placed at $f_\sharp = 30$). The averaged RPP growth rate overcomes the plane wave limit by a factor ∼2–3. This is consistent with the averaged speckle intensity $\langle I\rangle_{\mathrm{speckle}} = \int f_{\mathrm{speckle}}(I)I \, dI \simeq 3I_0$, where $\langle U\rangle_{\mathrm{speckle}} = \int f_{\mathrm{speckle}}(I)U \, dI$ and f_{speckle} is the speckle normalized distribution [60]. Additionally, the plain red lines illustrates $\langle\Gamma\rangle + \mathrm{Var}(\Gamma)^{1/2}$ [where $\mathrm{Var}(\Gamma) = \int_{\Gamma \geqslant -v_s}(\Gamma - \langle\Gamma\rangle)^2 P(\Gamma)d\Gamma$ is the variance of Γ] and shows that $\mathrm{Var}(\Gamma) \sim 1.2\langle\Gamma\rangle$, consistently with $[\langle I^2\rangle_{\mathrm{speckle}} - \langle I\rangle^2_{\mathrm{speckle}}]^{1/2} \simeq 1.2I_0$.

For a fixed f number of $f_\sharp = 8$ relevant for the NIF or the LMJ facilities, we explore the dependence of our predictions on the normalized Landau damping rate $\bar{v}$ and show that our model differs significantly from the usual plane wave predictions [see dashed dark line of Fig. 3(a)]. The averaged growth rate peaks around $\bar{v} \simeq 0.06$ while the plane wave growth rate is a constantly decreasing function. Additionally, the standard deviation remains of the order of the average growth rate most of the time, except in the high damping regime $\bar{v} \gtrsim 0.08$, where $\langle\Gamma\rangle$ vanishes and becomes negative.

III. TEMPORAL BSBS GROWTH

A. Comparison with paraxial hydrodynamical simulations

In order to confirm our predictions, we performed 3D Hera [48,49] simulations of a RPP beam propagating through a homogeneous He^{2+} plasma in the positive x direction with $\lambda_0 = 0.35$ μm, $I_0 = 2 \times 10^{14}$ W/cm^2, and a hyper-Gaussian transverse profile $I(y, z) \propto \exp[-(y^2 + z^2)^{5/2}/2u^5]$ at best focus with $u = 120$ μm and resulting in a focal spot with a flat averaged intensity within a circle of diameter $L_y \simeq 200$ μm. The electron and ion temperatures are $T_e = 2$ keV and $T_i = 1$ keV, respectively, with $n_e = 0.1 \, n_c$. The simulation domain is $\Delta x \times \Delta y \times \Delta z = 1 \times 0.4^2$ mm^3, with a mesh size of $dx = 1$ μm and $dy = dz = 0.3906$ μm and laser best focus localized at the center of the box, at $x = x_f = 500$ μm. The reflectivity, R, will be subsequently defined as the pump-to-backscattered instantaneous power ratio calculated at the laser injection position. Figure 4(a) shows the reflectivity exponential growth as predicted by Hera during which the value of $\mathrm{Im}(\omega)$ can be extracted [see the temporal derivative, Fig. 4(b)]; the obtained values are reported in Figs. 1(a) and 1(b) and 3(a) as black circles. Consistently with Ref. [50], significant fluctuations of the reflectivity growth are evidenced during the exponential growth of one simulation [see the red plain line in Fig. 4(b)] or when using two different RPP realizations [i.e., for two different sets of $\phi_\mathbf{k}$, Eq. (8), as plain and dashed lines in Fig. 4(b)]. We therefore reported, for each simulations, the averaged, minimum, and maximum values of $d_t \log(R)$ [where $d_t f$ designates the temporal derivative of $f(t)$] during the exponential growth as a circle, top and bottom of the error bars, respectively. Hence, the simulation points in Figs. 1(a) and 1(b) and 3(a) lie as expected around the maximum of the probability distribution (see the color map). More precisely, they lie between $\langle\Gamma\rangle$ (as a black plain line) and $\langle\Gamma\rangle + \mathrm{Var}(\Gamma)^{1/2}$ (as a plain red line). Our numerical results thus confirm the large variability $\langle\Gamma\rangle \sim \mathrm{Var}(\Gamma)^{1/2}$ of the BSBS growth for a low Landau damping rate [$\bar{v} = 0.0148$, Fig. 1(a)]. The increase
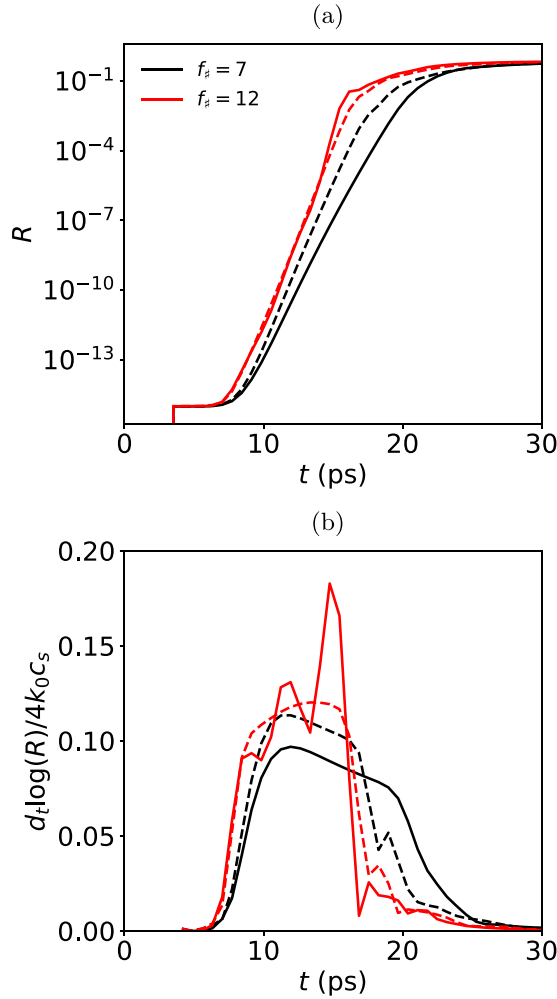
FIG. 4. (a), (b) Reflectivity and its normalized derivative extracted from 3D Hera simulations for the plasma parameters of Fig. 1(a) with $f_\sharp = 7$ (black lines) and $f_\sharp = 12$ (red lines). The plain and dashed lines correspond to two different RPP realizations, i.e., to different sets of RPP variables [$\phi_{\mathbf{k}}$, Eqs. (8) and (9)].

of $\bar{\nu}$ to 0.1, keeping the other plasma parameters unchanged [Fig. 1(b)], also confirms our predictions. In both Figs. 1(a) and 1(b), roughly 50% of the beam is described by a stable growth rate of $\Gamma \simeq -\nu_s$, hence, the resulting standard deviation is somewhat larger when $\nu_s/\omega_s = 0.1$ [Fig. 1(b)] than for $\nu_s/\omega_s = 0.0148$ [Fig. 1(a)]. Likewise, the circles in Fig. 3(a) are consistent with our predictions and evidence a relatively weak dependence of the temporal RPP growth rate on the acoustic Landau damping rate.

B. Validity of the convective BSBS model

The gain analysis, critical in ICF experiments design and interpretation [3,34,35,62], is based on the convective spatial growth rate derived in the plane wave limit. This regime is reached asymptotically at $t \gtrsim 25$ ps [see Fig. 4(a)], supposedly faster than the hydrodynamics timescale, after the BSBS has grown temporally. We now assess the impact of the speckle pattern on the spatial growth. The validity of the spatial growth equations [63] is based upon the abso-

lute stability of the system. Such a condition may remain blurry in a realistic situation where the laser is composed of numerous hot spots associated with a broad intensity distribution.

According to Ref. [64], we may estimate the frame velocity in which the instability grows preferentially through

$$V \simeq -\partial_{k_s} D / \partial_{\omega_s} D, \tag{29}$$

where D is given by Eq. (23). In the plane wave limit, this velocity is maximized around $V \simeq -0.5\,c$ below the absolute instability threshold and shows that acoustic wave packets preferentially grow upstream of the pump wave (against the laser injection boundary in a finite domain). When applied to our RPP dispersion relation, this velocity is completely deterministic and can be easily estimated. Hence, the use of Eq. (29) allows us to derive an objective criterion on the absolute stability of a given plasma, based on the fact that, when this velocity is vanishing, the acoustic fluctuations are amplified temporally and locally, the system is thus absolutely unstable which inherently leads to a violent nonlinear saturation. We may define the probability of absolute instability P_{abs}, which can be seen as the portion of the beam that is above absolute threshold, as the probability of having V below tens of its plane wave value,

$$P_{\mathrm{abs}} = \int_{|V| < c/20} p\, d\Gamma. \tag{30}$$

For both Figs. 1(a) and 1(b), $V \sim -c/2$ which implies $P_{\mathrm{abs}} = 0$, thus confirming the absolute stability of these systems. For a fixed f number of $f_\sharp = 8$, Fig. 3(b) suggests that when the plasma is weakly Landau damped ($\nu_s/\omega_s \lesssim 0.025$) and the laser "intense enough," a portion of the laser (here between 0.1% and 6%) is absolutely unstable. These predictions are compared with an independent speckle model, as inspired by Refs. [60,61], which estimates $P_{\mathrm{abs}} \simeq \int_{I > I_{\mathrm{abs}}} f_{\mathrm{speckle}}(I)dI$ (where I_{abs} is the absolutely unstable threshold and f_{speckle} the normalized speckle distribution). Illustrated as a black dotted line in Fig. 3(b), the independent-speckle model reproduces correctly the threshold $\bar{\nu} \sim 0.02$ below which $P_{\mathrm{abs}} > 0$. However, the portion of the beam as predicted by the dotted line rapidly reaches the absurd value of 100% because f_{speckle} is known to be ill defined in the low intensity part of the RPP beam, for $I \lesssim 2I_0$. Hence, Eq. (30) can enable to pinpoint the limit of the convective gain models and therefore the validity of the formalism of Refs. [35,36,63] more accurately than the existing independent-speckle estimates. We stress that the interplay between the convective and absolutely unstable speckles on the BSBS growth is out of the scope of this study.

IV. CONVECTIVE SPATIAL RPP BSBS AMPLIFICATION

The transport equation of the backscattered wave intensity I_d has been obtained in the plane wave limit in Refs. [36,63]. A similar equation is obtained for nonmonochromatic pump and scattered waves by performing a Fourier transform transversely to the main laser x direction and giving

$$-\partial_t I_d - v_g \partial_x I_d = J, \tag{31}$$

where $v_g = c\sqrt{1 - n_e/n_c}$ is the group velocity and the source term J reads as, with our notations,

$$J = -\frac{\omega_d \epsilon_0}{4} \text{Im}\left(E_p^{\star} \otimes \delta E \otimes \frac{\delta n_e}{n_c} \right). \tag{32}$$

The evaluation of the source term involves the use of Eqs. (A1) and (A3), written without the x-Fourier transform. We may first write

$$-\left(E_p^{\star} \otimes \frac{\delta n_e}{n_c} \right)_{\omega, \mathbf{k}} = \frac{n_e}{n_c} \frac{\epsilon_0 E_0^2}{N^2 2 n_c T_e} \sum_{\mathbf{k}_1} \sum_{\mathbf{k}_2} \times \left[e^{+i\Psi_{\mathbf{k}_1} - i\Psi_{\mathbf{k}_2}} \delta E(\omega, \mathbf{k} - \mathbf{k}_{0,1} + \mathbf{k}_{0,2}) \alpha_{k/f}\left(\frac{\omega - \omega_0}{|\mathbf{k} - \mathbf{k}_{0,1}|} \right) \right.$$

$$\left. + e^{-i\Psi_{\mathbf{k}_1} + i\Psi_{\mathbf{k}_2}} \delta E(\omega_s, \mathbf{k} + \mathbf{k}_{0,1} - \mathbf{k}_{0,2}) \alpha_{k/f}\left(\frac{\omega + \omega_0}{|\mathbf{k} + \mathbf{k}_{0,1}|} \right) \right], \tag{33}$$

where we have dropped the terms depending on $2\omega_0 \pm \omega$ and have used $\mathbf{k}_{0,1} = k_0 \hat{\mathbf{x}} + \mathbf{k}_1$, $\mathbf{k}_{0,2} = k_0 \hat{\mathbf{x}} + \mathbf{k}_2$, and $\Psi_{\mathbf{k}_1} = \phi_{\mathbf{k}_1} + \mathbf{k}_1^2 (x - x_f)/2k_0$. Keeping the Stokes component only (i.e., the first term in the square brackets) leads to

$$-\left(E_p^{\star} \otimes \frac{\delta n_e}{n_c} \right)_{\omega, \mathbf{k}} = \frac{1}{2} \frac{n_e}{n_c} \left(\frac{v_{\text{os}}}{v_{\text{the}}} \right)^2 \frac{1}{N} \sum_{\mathbf{k}_1} \sum_{\mathbf{k}_2} e^{+i\Psi_{\mathbf{k}_1} - i\Psi_{\mathbf{k}_2}} \delta E(\omega, \mathbf{k} - \mathbf{k}_{0,1} + \mathbf{k}_{0,2}) \alpha_{k/f}\left(\frac{\omega - \omega_0}{|\mathbf{k} - \mathbf{k}_{0,1}|} \right). \tag{34}$$

Proof can be made that for most high-energy laser facilities ($f_\sharp \sim 6$–10) and provided that $\bar{\nu} > 10^{-3}$, the width $\bar{\nu} c_s$ of the plasma resonance function $\text{Im}[\alpha_{k/f}(v_\phi)]$ is always larger than the variations $(\omega - \omega_0)/|\mathbf{k} - \mathbf{k}_{0,1}|$ due to $\mathbf{k}_1$. Hence, we may neglect the dependence on $\mathbf{k}_1$ of α_f in the above equation. In addition, we will approximate $\text{Im}[\alpha_{k/f}(v_\phi)]$ as in Eq. (18). The scattered wave intensity in the Fourier space $I_d(\mathbf{k}) = \epsilon_0 \delta E(\mathbf{k}) \otimes \delta E(\mathbf{k})^{\star}/2$ comes out of the combination of Eqs. (32) and (34), so that

$$J = \frac{n_e}{n_c} \left(\frac{v_{\text{os}}}{v_{\text{the}}} \right)^2 \frac{\omega_d}{4} \text{Im}[\alpha_f(c_s)]$$

$$\times \frac{1}{N} \sum_{\mathbf{k}_1} \sum_{\mathbf{k}_2} e^{+i\Psi_{\mathbf{k}_1} - i\Psi_{\mathbf{k}_2}} I_d(\mathbf{k}_d - \mathbf{k}_{0,1} + \mathbf{k}_{0,2}). \tag{35}$$

Assuming that the scattered wave has the same f-cone angle as the pump wave $I_d \propto \text{H}(2k_m - |k_\perp|)$ yields

$$J = \frac{n_e}{n_c} \left(\frac{v_{\text{os}}}{v_{\text{the}}} \right)^2 \frac{\omega_d}{4} \text{Im}[\alpha_f(c_s)] I_d \bar{S},$$

$$\bar{S} = \frac{1}{N} \sum_{\mathbf{k}_1} \sum_{\mathbf{k}_2} e^{+i\phi_{\mathbf{k}_1} - i\phi_{\mathbf{k}_2} + i\frac{\mathbf{k}_1^2 - \mathbf{k}_2^2}{2k_0}(x - x_f)}. \tag{36}$$

The random variable $\bar{S}$ may be approximated to a normal law using the central limit theorem. Although the calculations are feasible off focus, we set subsequently $x = x_f$, thus restraining the following analysis to the vicinity of the pump wave focal plane. Hence, we use $\bar{S} \simeq N \sum_{\mathbf{k}_1, \mathbf{k}_2} \exp(i\phi_{\mathbf{k}_1} - i\phi_{\mathbf{k}_2})$ so that Eq. (31) may be recast as

$$-\partial_t I_d - v_g \partial_x I_d = v_g \mathcal{K} I_d \mathcal{N}(1, 2), \tag{37}$$

$$\mathcal{K} = \frac{n_e}{n_c} \left(\frac{v_{\text{os}}}{v_{\text{the}}} \right)^2 \frac{\omega_d}{4 v_g} \text{Im}[\alpha_f(c_s)], \tag{38}$$

where $\mathcal{K}$ is the spatial convective growth rate which coincides with the well known plane wave result and $\mathcal{N}(1, 2)$ is the random normal law centered in unity, of variance two, and independent of time and position (t, x) (since $\partial_t \phi_{\mathbf{k}_{1/2}} =$

$\partial_x \phi_{\mathbf{k}_{1/2}} = 0$). Unlike the temporal growth (see Sec. III) where a large variance appears in the RPP dispersion relation ($=N$), the variability in the convective case is much smaller. Indeed, when considering the spatial BSBS amplification [thus removing the temporal derivative in Eq. (31)], we assume that the scattered wave propagation covers many speckles, thus reducing the speckle randomness of the resulting gain. However, when increasing the number of phase plate elements, the gain variance remains strictly positive, showing that even for very large beams propagating in a homogeneous plasma, a finite randomness of the spatial growth is to be expected.

We now introduce $\langle I_d \rangle_y$, the y-averaged (over -100 μm$<$ $y < 100$ μm) scattered intensity in the plane $z = 0$. The late time convective growth rate has been extracted from our Hera simulation by averaging $-d_x \log(\langle I_d \rangle_y)$ over the first 200 μm of the simulation domain of Fig. 3(a) and gathered in Fig. 3(c) as circles. A good agreement is obtained above $\bar{\nu} \sim 0.05$ when confronted with the averaged theoretical predictions of Eq. (38) (as a plain line) or with 1D Hera simulation results (crosses). In addition, Ref. [46] relates the BSBS spatial growth to two contributions. The first one, named the "collective" growth, is found to be stable for our plasma and laser parameters. The second "RPA-like" contribution yields similar predictions than our statistically averaged spatial growth rate, Eq. (38). We therefore confirm the weak impact of a RPP on the *averaged* convective BSBS growth, at least for ICF-like parameters (i.e., $T_e \sim [1$–5$]$ keV, $I \sim 10^{13}$–10^{16} W/cm^2, $\bar{\nu} \gtrsim 0.007$).

When the acoustic wave damping rate is small, a strong BSBS growth is obtained leading to the pump depletion and resulting in a smaller effective spatial gain than predicted by our linear dispersion relations. The convective gain saturation, as extracted from our simulations, occurs in both 3D and 1D simulations at $\mathcal{K} \times 1$ mm $\simeq 20$ and 30, respectively. This is consistent with the fact that the RPP BSBS is effectively driven locally in speckles of intensities larger than the averaged beam intensity, thus suggesting that the local hot spot spatial amplification is larger than the gain averaged over the whole beam.

V. PREDICTING THE REFLECTIVITY OF A RPP BEAM

A. Reflectivity in the plane wave framework

The so-called Tang model gives an implicit formula that relates the noise level (R_0), the spatial gain (G), and the asymptotic reflectivity level (R) [65]:

$$R(1 - R) = R_0 \exp[(1 - R)G] - R_0 R. \qquad (39)$$

Although this model is based on the strong assumption that the saturation mechanism is solely driven by the pump depletion, it helps to estimate the expected reflectivity level. The seed level, in all the simulations presented here, is imposed to $I_{d0} = R_0 I_0$ with $R_0 = 10^{-16}$. Note that the seed reflectivity used in our simulations is smaller than the one expected physically, given by Eq. (46) subsequently. Hence, the reflectivity resulting from the spatial growth rates as illustrated in Fig. 3(b) should be trustworthy, at least in the domain where nonlinear effects are negligible, say below $R < 0.1$. Indeed, a good agreement is evidenced in Fig. 5(a) when comparing the 1D Hera asymptotic reflectivity (as red crosses) with Tang's model applied on the plane wave convective gain (see the a plain red line). Unfortunately, a mismatch of more than an order of magnitude is obtained when comparing these theoretical predictions with the RPP numerical result [see red circles in Fig. 5(a)]. Similar discrepancies with experimental measurements have been characterized and ascribed to the hot spot dynamics lacking from the plane wave theory [see, for example, Fig. 7 of Ref. [63] and Ref. [66]]. Reference [38] presents an interesting theory [see red dotted line in Fig. 5(a)], based on the independent-speckle assumption, which also largely disagrees with the RPP Hera reflectivity.

B. Reflectivity of a RPP beam and paraxial fluid simulations

In order to understand the discrepancies between the plane wave predictions [65] and the reflectivity as given by our paraxial simulations, we address the impact of the normal random law in Eq. (37) (that results from the random speckle distribution) onto the backscattering level. Note that the random factor $\mathcal{N}(1, 2)$ implies that $\langle R \rangle \propto \exp(\langle G \rangle)$ no longer holds, even without any nonlinear effects. Applying the same procedure as Eq. (27), we may reconstruct the reflectivity probability distribution by binning the reflectivity such that $R_n = R_0 + n\,dR \leqslant 1$, where n is a positive integer and dR the bin width. Solving Tang's implicit equation with the seed $R_0 I_0$, the pump initial intensity I_0 and the effective gain $G = \mathcal{K} L_x X$ where X is a real associated with the Gaussian probability [$\mathcal{N}(1, 2)$], we obtain the reflectivity $R(X)$ from which derives the reflectivity probability distribution [similarly to Eq. (27)]

$$\bar{p}(R_n) = \frac{dP}{dR}(R_n) = \sum_{R_n < R(X) < R_{n+1}} \frac{e^{-(X-1)^2/4}}{\sqrt{4\pi}} \frac{dX}{dR}. \qquad (40)$$

The resulting probability distribution is well converged by discretizing the interval $X \in [-3 \times 2^{1/2}, 3 \times 2^{1/2}]$ in 6000 regularly spaced elements. Illustrated as a color map in Fig. 5(a), $\bar{p}$ exhibits a local maximum which is in excellent agreement with the simulation results. As for the growth rate probability distribution, the probability absolute maximum lies around $R = R_0 = 10^{-16}$ (not shown) and corresponds to all the values of the random variable X too weak to explain the
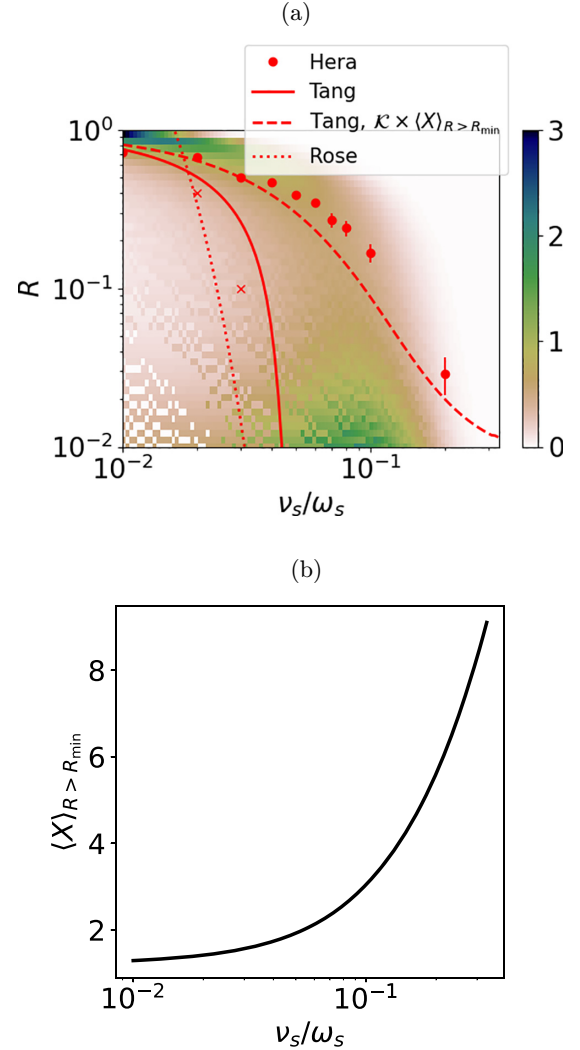

FIG. 5. (a) Asymptotic reflectivity as predicted by 1D (crosses) and 3D RPP (circle) Hera simulations. The error bars correspond to the standard deviation measured over 50 ps. The model of Ref. [65] [Eq. (39)] with a plane wave gain, Eq. (44), corresponds to the plain line. The thick dashed line is obtained by using the RPP gain given by Eq. (45), $G \equiv G_{\mathrm{RPP}} = \langle X \rangle_{R>R_{\min}} \mathcal{K} \times 1$ mm with $R_{\min} = 10^{-2}$. The reflectivity, as predicted by Eq. (9) of Ref. [38], is superimposed as a dotted line. The color map is the probability distribution of the asymptotic reflectivity, as predicted by Eq. (40) which is, by construction, normalized to unity, i.e., $\int_0^1 \bar{p}\,dR = 1$. (b) Value of $\langle X \rangle_{R(X)>R_{\min}}$ as predicted by Eqs. (42) and (43). The plasma and laser parameters are identical to Fig. 3. The plasma response is here fluid [see Eq. (5)].

~14 to 15 orders of magnitude of amplification factor required to reach $R \sim 0.01$–0.1 ($G = \mathcal{K} L_x X \lesssim 30$), as observed in our simulations. Due to the presence of the speckles, X may be larger than unity which leads to a measurable reflectivity in agreement with Hera. Introducing a minimum reflectivity value below which the BSBS is considered negligible, $R_{\min}$, we estimate the averaged value of X over the region $R > R_{\min}$:

$$\langle X \rangle_{R(X)>R_{\min}} = \frac{\int_{R(X)>R_{\min}} X e^{-(X-1)^2/4} dX}{\int_{R(X)>R_{\min}} e^{-(X-1)^2/4} dX}. \qquad (41)$$

The denominator and the numerator can be directly related to $X_{\min}$, the random variable value above which $R > R_{\min}$. For $R_{\min} \lesssim 10^{-2}$, we have, $R_{\min} \simeq R_0 e^{\mathcal{K}L X_{\min}}$ and we obtain

$$\langle X \rangle_{R(X) > R_{\min}} = \frac{1 + \mathrm{erf}\left(\frac{1-X_{\min}}{2}\right) + \frac{2e^{-(X_{\min}-1)^2/4}}{\sqrt{\pi}}}{1 + \mathrm{erf}\left(\frac{1-X_{\min}}{2}\right)}, \quad (42)$$

$$X_{\min} \simeq \frac{1}{\mathcal{K}L_x} \log\left(\frac{R_{\min}}{R_0}\right), \quad (43)$$

where erf is the error function. Figure 5(b) illustrates as a thick black line the dependence of $\langle X \rangle_{R(X) > R_{\min}}$ on $\bar{\nu}$ when $R_{\min} = 10^{-2}$ and demonstrates that it ranges from ~ 1.9 to ~ 10 as $\bar{\nu}$ increases from 10^{-2} to 0.2. The plane wave reflectivity with depletion is obtained by extracting numerically R from Tang's implicit equation [Eq. (39)] where

$$G \equiv G_{\mathrm{PW}} = \mathcal{K}L_x \quad (44)$$

is the plane wave gain of our system. For a RPP beam, we propose to use a similar procedure with

$$G \equiv G_{\mathrm{RPP}} = \langle X \rangle_{R(X) > R_{\min}} \mathcal{K}L_x. \quad (45)$$

Hence, when solving Tang's equation with the above gain, we multiply the pump averaged intensity by $\langle X \rangle_{R(X) > R_{\min}}$. The best fit to our paraxial simulations corresponds to $R_{\min} = 10^{-2}$ and is in very good agreement with the numerical data [see the thick dashed red line in Fig. 5(a)]. Hence, the quantity $I_0 \langle X \rangle_{R(X) > R_{\min}}$ corresponds to the intensity of the speckle population that is the more likely to drive the reflectivity and it can easily be estimated in any convective gain analysis. In other words, a BSBS reflectivity of a RPP beam is estimated here by replacing the averaged intensity I_0 by $I_0 \langle X \rangle_{R(X) > R_{\min}}$ inside equations obtained in the plane wave limit.

However, the corresponding reflectivity is by construction always above $R_{\min}$ which means that our analytical model is wrong as soon as it predicts $R \lesssim R_{\min}$. This represents a simple and efficient improvement of the plane wave predicting capabilities that accounts for RPP and constitutes a promising route for accurately modeling the amount of backscattering in ICF or more generally in high-energy density experiments.

C. Comparison with experimental measurements

Brillouin backscattering measurements have been performed in a fairly homogeneous plasma [68] probed and controlled by Thomson scattering [67]. Such data have been used to test numerical prediction capabilities [69]. Figure 6 confronts our RPP BSBS reflectivity model as a black plain line with the experimental measurements as black squares (RPP). According to the experiment and probably due to the large acoustic Landau damping of the plasma, the use of SSD does not seem to affect the measured reflectivity. However, for sake of consistency, we will ignore the RPP + SSD data subsequently. In the experiment, the cavity is filled with 30% of CH_4 and 70% of C_3H_8 at one atmosphere and is irradiated by heater beams, leading after 700 ps to a 1.5-mm-long homogeneous electron density along the interaction beam path of $n_e \simeq 0.06 \, n_c$ and an electron temperature of $T_e \simeq 2.7$ keV.

The reflectivity seed level (R_0) is related to the spontaneous emission of the ion acoustic waves in a single speckle ϵ_B,
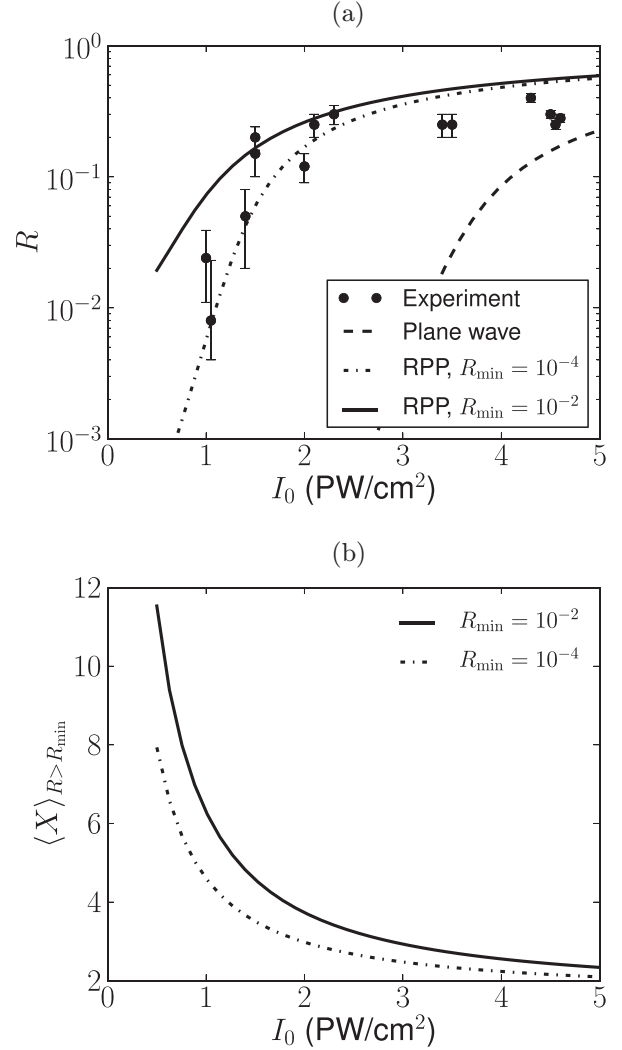

FIG. 6. (a) Reflectivity as measured experimentally [67–69]. The theoretical calculations have been performed with laser and plasma parameters detailed in Sec. VII of Ref. [63] and a noise level given by Eq. (46). The plane wave and RPP reflectivities in black lines correspond to Tang's formula (39) solved numerically for a plane wave [Eq. (44)] and a RPP [Eq. (45)] gain, respectively. The plasma length is $L_x = 1.5$ mm and the seed is given by Eq. (46). The plasma response is treated here kinetically [see Eq. (6)]. (b) Value of Eq. (41) for $R_{\min} = 10^{-2}$ and $R_{\min} = 10^{-4}$.

through $R_0 = \epsilon_B / I_0 \pi (f_\sharp \lambda_0)^2$. The value of ϵ_B can be obtained from Eq. (6) of Ref. [70], which can be estimated here using the averaged ion charge and mass number (here, $\langle Z \rangle \simeq 2.3$, $\langle A \rangle \simeq 3.9$) and leading to

$$R_0 = \frac{1}{\pi} \frac{\omega_0 T_e}{1 - n_e/n_c} \frac{1 + \langle Z \rangle Q}{1 + \langle Z \rangle Q T_e/T_i} \frac{1}{I_0 \pi (f_\sharp \lambda_0)^2},$$

$$Q = \sqrt{\frac{T_e m_i}{T_i m_e}} e^{-\frac{\langle Z \rangle T_e}{T_i} - \frac{3}{2}}. \quad (46)$$

For the experimental parameters addressed here, it scales as $R_0 \sim 10^{-9}$. Choice has been made to set $T_i = T_e/2$. As the plasma is composed of carbon and hydrogen ions, the plasma

response will be treated kinetically [Eq. (6)]. The sound speed will be associated hereafter as the phase speed value that maximizes $\text{Im}[\alpha_k(v_\phi)]$.

Hence, the reflectivity obtained by feeding the plain wave gain $\mathcal{K} \times 1.5$ mm to Tang's formula [Eq. (39), solution illustrated as a dashed black line in Fig. 6(a)] greatly underestimates the experimental values by a few orders of magnitude and for beam energies below 4 PW/cm^2. When using the gain of Eq. (45) [see Fig. 6(b)] before calculating the reflectivity (see the black plain line for $R_{\min} = 10^{-2}$), a much better agreement is found. The dependence of our model on $R_{\min}$ is illustrated by the black dotted-dashed lines for which $R_{\min} = 10^{-4}$, and in good agreement with the experimental data, especially below 1.5 PW/cm^2. Indeed, the dependence of Eq. (41) on $R_{\min}$ is directly related to the finite statistical variability of R, as discussed and illustrated in Sec. V B. In particular, the convective amplification of slightly unstable systems (i.e., $R \lesssim 0.05$) relies on the hottest and rarest speckles [$\langle X \rangle_{R>R_{\min}} > 5$ for intensities $\lesssim 1$ PW/cm^2, see Fig. 6(b)]. Hence, small reflectivities are associated with a significant statistical variability and causing significant dependence of $\langle X \rangle_{R>R_{\min}}$ on $R_{\min}$. Above ~ 2.5 PW/cm^2, the dependence of our results on $R_{\min}$ vanishes as $\langle X \rangle_{R>R_{\min}}$ decreases to ~ 2. In addition, the nonlinear effects not included in Tang's model should explain the saturation of the experimental reflectivity to $\sim 20\%$–40% while our predictions continue to grow up to $\sim 60\%$ at 5 PW/cm^2. Note that Eq. (30) predicts $P_{\text{abs}} = 0$ so that an absolute instability cannot be the main cause of the discrepancy at large laser beam energy between the theory and the experiment [see Fig. 6(a)].

VI. CONCLUSION

Unlike previous studies where the well known speckle distribution in vacuum is used to extend the plane wave calculations to a RPP beam, our derivation of the wave mixing equations starts from the proper RPP fields. This allows to avoid any assumption on the acoustic wave damping rate and reveal the importance of the phase plate variability.

We have first developed a BSBS dispersion relation that accounts for the RPP cone angle opening and randomness. Comparison with 3D paraxial results confirms that the presence of the speckles significantly changes the temporal reflectivity growth and demonstrates that modeling the phase plate variability is critical to quantitatively understand the temporal BSBS growth.

Notably, the absolute-instability criterion is deterministic for a plane wave whereas it is speckle dependent for a RPP beam. Our model also gives access to a quantitative observable [Eq. (30)] that allows to estimate the portion of the beam which is absolutely unstable. thus helping to assess the limit of the convective gain analysis on which many BSBS studies are based.

We have also demonstrated that, although the averaged convective BSBS gain (of the transversely averaged beam) remains similar for a RPP beam or a plane wave, the amount of backscattering is affected by the use of spatial smoothing. Indeed, when applying a statistical average of Eq. (37), the covariance between the scattered intensity and the spa-

tial growth rate random variable appears in the right-hand side and explains the difference between a RPP and a plane wave BSBS spatial amplification. The resulting reflectivity, modeled in this study according to Ref. [65], is significantly increased by the use of a RPP, especially when the plane wave analysis points to a nearly stable system. In this case, the observed RPP Hera reflectivity corresponds very well with the maximum of the reflectivity probability distribution obtained with an accurate modeling of the BSBS spatial amplification of a spatially smoothed beam. We have then deduced a simple analytical formula which estimates the speckle intensity that is more likely to drive a significant reflectivity. When using this prediction as a correction to the plane wave convective gain and to the Tang's reflectivity model, a very good agreement with our RPP numerical reflectivity is obtained.

Including an idealized polarization smoothing in the present analysis could simply correspond to dividing the averaged laser intensity I_0 by a factor 2 and multiply the initial seed by a factor 2. Temporal smoothing, however, is much more challenging to include in the present model and is known to affect the BSBS, at least in weakly Landau damped plasmas [44]. In addition, the effect of nonhomogeneity has been neglected and should be accounted for when addressing a realistic situation or gas jet experiments [70,71]. The use of the central limit theorem (see Sec. III or in Sec. IV) assumes a large number of phase plate elements ($\gtrsim 30$), i.e., a wide enough laser focal spot, which also adds a constraint on the hydrodynamic scale length ($L_h \simeq n_e T_e / |\nabla n_e T_e|$). In a nonhomogeneous plasma, the correction to the plane wave spatial amplification [Eqs. (37), (42), and (43)] remains valid locally if at least 30 phase plate elements may be found in a region of space where density gradients are negligible, i.e., if $L_h \gtrsim 30 f_\sharp \lambda_0$. Except from the depletion of the pump, the present analysis does not include any of the nonlinear effects [72,73] that are likely essential for accurately predicting the high convective gain systems or when a significant part of the beam is absolutely unstable.

Importantly, the interplay between BSBS and other laser-plasma interaction effects such as beam bending, cross beam energy transfer has been neglected so far. The so-called plasma smoothing effects [74,75] are known to decrease the effective $f_\sharp$ value, which should alleviate sensibly the BSBS temporal growth [see Figs. 1(a) and 1(b)]. However, the asymptotic reflectivity of interest for ICF experiments is preferentially driven by the spatial amplification which remains, independent of $f_\sharp$, at least in the vicinity of the focal plane (see Sec. IV). This seems to contrast with the results of Ref. [76] where proof is made that plasma smoothing does reduce the amount of BSBS. This suggests that restricting the convective analysis in the vicinity of the focal spot [i.e., setting $x = x_f$ in Eq. (36)] might not be appropriate when addressing the interaction between backward and forward stimulated Brillouin scatter.

Finally, the analytical correction to the plane wave spatial amplification model introduced in Sec. V paves the way for realistic laser-plasma instability models, thus improving the predicting capabilities of hydrodynamic codes for the design and interpretation of ICF and high-energy density physics experiments.

APPENDIX A: DERIVATION OF EQ. (17)

We start with the fields of Eq. (8), written in the Fourier space $(\omega_p, \mathbf{k}_p)$ and enveloped in space and time around $(\omega_0, k_0 \hat{\mathbf{x}})$. We then obtain

$$E_p(\omega_p, \mathbf{k}_p) = \frac{E_0}{N} \sum_{\mathbf{k}_1} [e^{i\Psi_{\mathbf{k}_1}} \delta(\omega_p - \omega_0, \mathbf{k}_p - \mathbf{k}_{0,1})$$

$$+ e^{-i\Psi_{\mathbf{k}_1}} \delta(\omega_p + \omega_0, \mathbf{k}_p + \mathbf{k}_{0,1})], \qquad (A1)$$

$$\Psi_{\mathbf{k}_1} = \phi_{\mathbf{k}_1} + \frac{\mathbf{k}_1^2 x_f}{2k_0}. \qquad (A2)$$

Hence, injecting it into Eq. (4), and in Maxwell equations linearized around the scattered field amplitude, i.e., $\delta E(\omega_d, \mathbf{k}_d)$, we obtain

$$\frac{\delta n_e}{n_e}(\omega_s, \mathbf{k}_s) = - \alpha_{f/k}(v_\phi) \frac{\epsilon_0 E_0}{N 2 n_c T_e}$$

$$\times \sum_{\mathbf{k}_1} [e^{i\Psi_{\mathbf{k}_1}} \delta E(\omega_s - \omega_0, \mathbf{k}_s - \mathbf{k}_{0,1})$$

$$+ e^{-i\Psi_{\mathbf{k}_1}} \delta E(\omega_s + \omega_0, \mathbf{k}_s + \mathbf{k}_{0,1})] \qquad (A3)$$

and

$$(\omega_d^2 - \omega_{pe}^2 - \mathbf{k}_d^2 c^2) \delta E(\omega_d, \mathbf{k}_d)$$

$$= \frac{\omega_0^2}{2N} E_0 \sum_{\mathbf{k}_2} \left[e^{i\Psi_{\mathbf{k}_2}} \frac{\delta n_e}{n_c}(\omega_d - \omega_0, \mathbf{k}_d - \mathbf{k}_{0,2}) \right.$$

$$\left. + e^{-i\Psi_{\mathbf{k}_2}} \frac{\delta n_e}{n_c}(\omega_d + \omega_0, \mathbf{k}_d + \mathbf{k}_{0,2}) \right], \qquad (A4)$$

respectively.

Combining the two above equations and dropping the terms $\delta n_e(\omega_s \pm 2\omega_0)$ as $\omega_0 \gg \omega_s$, we also retain the usual stoke light branch only:

$$\frac{\delta n_e}{n_e}(\omega_s, \mathbf{k}_s) = - \alpha_{k/f}(v_\phi) \frac{n_e}{n_c} \frac{\epsilon_0 E_0^2}{2 n_c T_e} \frac{\omega_0^2}{2N^2}$$

$$\times \sum_{\mathbf{k}_1} \sum_{\mathbf{k}_2} \frac{e^{i\Psi_{\mathbf{k}_1} - i\Psi_{\mathbf{k}_2}}}{D_-(\mathbf{k}_{0,1})} \frac{\delta n_e}{n_e}(\omega_s, \mathbf{k}_s - \mathbf{k}_{0,1} + \mathbf{k}_{0,2}). \qquad (A5)$$

Seeking for monochromatic growth of the acoustic fluctuations, so that $\delta n_e(\omega, \mathbf{k}) \propto \delta(\omega - \omega_s, \mathbf{k} - \mathbf{k}_s)$, and after integration, we obtain Eq. (17).

APPENDIX B: EXACT NUMERICAL RESOLUTION OF THE RPP DISPERSION RELATION

The numerical resolution of the dispersion relation, Eqs. (22) or (23), used to validate the approximation of Eq. (26), is inspired from the graphical solver detailed in Ref. [77]. We first evaluate $\text{Im}(D)$, where D is given by Eq. (23), on a carefully chosen grid lying in the $[k_{sx}, \text{Im}(\omega_s)]$ plane and setting $\text{Re}(\omega_s) = k_{sx} c_s / g$. The solutions of $D = 0$ are then extracted by detecting the change of sign of $\text{Re}(D)$ while following the locus $\text{Im}(D) = 0$. The precision of this scheme is given by the chosen grid on which D is evaluated and can be improved by feeding the obtained solutions as a guess of a nonlinear solver.

[1] C. Courtois, C. Robert, D. Bretheau, J. Fariaut, M. Ferri, I. Geoffray, G. Legay, F. Philippe, R. Rosch, G. Soullie *et al.*, Phys. Plasmas **28**, 073301 (2021).

[2] M. Primout, L. Jacquet, L. Lecherbourg, L. Videau, P.-E. Masson-Laborde, B. Villette, G. Legay, and L. Le-Deroff, Phys. Plasmas **29**, 073302 (2022).

[3] J. D. Lindl, P. Amendt, R. L. Berger, S. G. Glendinning, S. H. Glenzer, S. W. Haan, R. L. Kauffman, O. L. Landen, and L. J. Suter, Phys. Plasmas **11**, 339 (2004).

[4] A. Zylstra, O. Hurricane, and D. Callahan, Nature (London) **601**, 542 (2022).

[5] W. Zheng, X. Wei, Q. Zhu, F. Jing, D. Hu, X. Yuan, W. Dai, W. Zhou, F. Wang, D. Xu *et al.*, Matter Radiat. Extremes **2**, 243 (2017).

[6] K. Lan, Y. Dong, J. Wu, Z. Li, Y. Chen, H. Cao, L. Hao, S. Li, G. Ren, W. Jiang *et al.*, Phys. Rev. Lett. **127**, 245001 (2021).

[7] A. Casner, T. Caillaud, S. Darbon, A. Duval, I. Thfouin, J. Jadaud, J. LeBreton, C. Reverdin, B. Rosse, R. Rosch *et al.*, High Energy Density Phys. **17**, 2 (2015).

[8] R. P. Drake, *Introduction to High-Energy-Density Physics* (Springer, Berlin, 2006), pp. 1–17.

[9] G. Schurtz, S. Gary, S. Hulin, C. Chenais-Popovics, J.-C. Gauthier, F. Thais, J. Breil, F. Durut, J.-L. Feugeas, P.-H. Maire *et al.*, Phys. Rev. Lett. **98**, 095002 (2007).

[10] C. Rousseaux, M. Rabec le Gloahec, S. D. Baton, F. Amiranoff, J. Fuchs, L. Gremillet, J. C. Adam, A. Héron, and P. Mora, Phys. Plasmas **9**, 4261 (2002).

[11] B. J. MacGowan, B. B. Afeyan, C. A. Back, R. L. Berger, G. Bonnaud, M. Casanova, B. I. Cohen, D. E. Desenne, D. F. DuBois, A. G. Dulieu *et al.*, Phys. Plasmas **3**, 2029 (1996).

[12] D. S. Montgomery, B. B. Afeyan, J. A. Cobble, J. C. Fernández, M. D. Wilke, S. H. Glenzer, R. K. Kirkwood, B. J. MacGowan, J. D. Moody, E. L. Lindman *et al.*, Phys. Plasmas **5**, 1973 (1998).

[13] S. Hüller, G. Raj, W. Rozmus, and D. Pesme, Phys. Plasmas **27**, 022703 (2020).

[14] J. D. Moody, B. J. MacGowan, D. E. Hinkel, W. L. Kruer, E. A. Williams, K. Estabrook, R. L. Berger, R. K. Kirkwood,

D. S. Montgomery, and T. D. Shepard, Phys. Rev. Lett. **77**, 1294 (1996).

[15] D. E. Hinkel, E. A. Williams, and C. H. Still, Phys. Rev. Lett. **77**, 1298 (1996).

[16] A. J. Schmitt and B. B. Afeyan, Phys. Plasmas **5**, 503 (1998).

[17] M. Grech, V. T. Tikhonchuk, G. Riazuelo, and S. Weber, Phys. Plasmas **13**, 093104 (2006).

[18] Y. Kato, K. Mima, N. Miyanaga, S. Arinaga, Y. Kitagawa, M. Nakatsuka, and C. Yamanaka, Phys. Rev. Lett. **53**, 1057 (1984).

[19] S. Skupsky, R. W. Short, T. Kessler, R. S. Craxton, S. Letzring, and J. M. Soures, J. Appl. Phys. **66**, 3456 (1989).

[20] J. Garnier, Phys. Plasmas **6**, 1601 (1999).

[21] J. Garnier and L. Videau, Phys. Plasmas **8**, 4914 (2001).

[22] M. Duluc, D. Penninckx, P. Loiseau, G. Riazuelo, A. Bourgeade, A. Chatagnier, and E. D'Humières, Phys. Plasmas **26**, 042707 (2019).

[23] D. E. Hinkel, E. A. Williams, R. L. Berger, L. V. Powers, A. B. Langdon, and C. H. Still, Phys. Plasmas **5**, 1887 (1998).

[24] J. Myatt, D. Pesme, S. Hüller, A. Maximov, W. Rozmus, and C. E. Capjack, Phys. Rev. Lett. **87**, 255003 (2001).

[25] S. H. Glenzer, D. H. Froula, L. Divol, M. Dorr, R. L. Berger, S. Dixit, B. A. Hammel, C. Haynam, J. A. Hittinger, J. P. Holder *et al.*, Nat. Phys. **3**, 716 (2007).

[26] C. Labaune, Nat. Phys. **3**, 680 (2007).

[27] P. Michel, L. Divol, E. A. Williams, S. Weber, C. A. Thomas, D. A. Callahan, S. W. Haan, J. D. Salmonson, S. Dixit, D. E. Hinkel *et al.*, Phys. Rev. Lett. **102**, 025004 (2009).

[28] C. Neuville, C. Baccou, A. Debayle, P.-E. Masson-Laborde, S. Hüller, M. Casanova, D. Marion, P. Loiseau, K. Glize, C. Labaune *et al.*, Phys. Rev. Lett. **117**, 145001 (2016).

[29] S. Hüller, G. Raj, M. Luo, W. Rozmus, and D. Pesme, Philos. Trans. R. Soc. London A **378**, 20200038 (2020).

[30] A. Oudin, A. Debayle, C. Ruyer, and D. Bénisti, Phys. Rev. Lett. **127**, 265001 (2021).

[31] H. A. Rose and P. Mounaix, Phys. Plasmas **18**, 042109 (2011).

[32] C. Rousseaux, K. Glize, S. D. Baton, L. Lancia, D. Bénisti, and L. Gremillet, Phys. Rev. Lett. **117**, 015002 (2016).

[33] V. T. Tikhonchuk, T. Gong, N. Jourdain, O. Renner, F. P. Condamine, K. Q. Pan, W. Nazarov, L. Hudec, J. Limpouch, R. Liska *et al.*, Matter Radiat. Extremes **6**, 025902 (2021).

[34] S. Laffite and P. Loiseau, Phys. Plasmas **17**, 102704 (2010).

[35] D. J. Strozzi, D. S. Bailey, P. Michel, L. Divol, S. M. Sepke, G. D. Kerbel, C. A. Thomas, J. E. Ralph, J. D. Moody, and M. B. Schneider, Phys. Rev. Lett. **118**, 025002 (2017).

[36] A. Debayle, C. Ruyer, O. Morice, P.-E. Masson-Laborde, P. Loiseau, and D. Benisti, Phys. Plasmas **26**, 092705 (2019).

[37] R. L. Berger, C. A. Thomas, K. L. Baker, D. T. Casey, C. S. Goyon, J. Park, N. Lemos, S. F. Khan, M. Hohenberger, J. L. Milovich *et al.*, Phys. Plasmas **26**, 012709 (2019).

[38] H. A. Rose and D. F. DuBois, Phys. Rev. Lett. **72**, 2883 (1994).

[39] L. Divol and P. Mounaix, Phys. Plasmas **6**, 4037 (1999).

[40] L. Divol and P. Mounaix, Phys. Plasmas **6**, 4049 (1999).

[41] V. T. Tikhonchuk, P. Mounaix, and D. Pesme, Phys. Plasmas **4**, 2658 (1997).

[42] V. T. Tikhonchuk, S. Hüller, and P. Mounaix, Phys. Plasmas **4**, 4369 (1997).

[43] S. Hüller, A. Porzio, and J. Robiche, New J. Phys. **15**, 025003 (2013).

[44] L. Divol, Phys. Rev. Lett. **99**, 155003 (2007).

[45] B. Brandão, J. E. Santos, R. M. G. M. Trines, R. Bingham, and L. O. Silva, Plasma Phys. Controlled Fusion **63**, 094003 (2021).

[46] A. O. Korotkevich, P. M. Lushnikov, and H. A. Rose, Phys. Plasmas **22**, 012107 (2015).

[47] C. Ruyer, A. Debayle, P. Loiseau, P. E. Masson-Laborde, J. Fuchs, M. Casanova, J. R. Marquès, L. Romagnani, P. Antici, N. Bourgeois *et al.*, Phys. Plasmas **28**, 052701 (2021).

[48] H. Jourdren, Hera: A hydrodynamic amr platform for multiphysics simulations, in *Adaptive Mesh Refinement - Theory and Applications*, edited by T. Plewa, T. Linde, and V. Gregory Weirs (Springer, Berlin, 2005), pp. 283–294.

[49] P. Loiseau, O. Morice, D. Teychenné, M. Casanova, S. Hüller, and D. Pesme, Phys. Rev. Lett. **97**, 205001 (2006).

[50] P. Mounaix and L. Divol, Phys. Rev. Lett. **89**, 165005 (2002).

[51] W. L. Kruer, *The Physics Of Laser Plasma Interactions* (Addison-Wesley, Boston, 1988).

[52] C. Ruyer, A. Debayle, P. Loiseau, M. Casanova, and P. E. Masson-Laborde, Phys. Plasmas **27**, 102105 (2020).

[53] J. F. Drake, P. K. Kaw, Y. C. Lee, G. Schmid, C. S. Liu, and M. N. Rosenbluth, Phys. Fluids **17**, 778 (1974).

[54] B. D. Fried, M. Gell-Mann, J. D. Jackson, and H. W. Wyld, J. Nucl. Energy, Part C: Plasma Phys. **1**, 190 (1960).

[55] H. A. Rose and S. Ghosal, Phys. Plasmas **5**, 1461 (1998).

[56] J. E. Rothenberg, J. Opt. Soc. Am. B **14**, 1664 (1997).

[57] L. Videau, C. Rouyer, J. Garnier, and A. Migus, J. Opt. Soc. Am. A **16**, 1672 (1999).

[58] H. A. Rose, Phys. Plasmas **3**, 1709 (1996).

[59] H. A. Rose and D. F. DuBois, Phys. Fluids B **5**, 590 (1993).

[60] L. Divol, Une Modélisation analytique de la réflectivité d'un faisceau laser lissé temporellement : instabilités paramétriques de rétrodiffusion et modèles de points chauds indépendants, PhD. thesis, Centre de Physique Théorique, Ecole Polytechnique, 91128 Palaiseau Cedex, France, 1999.

[61] G. Cristoforetti, S. Hüller, P. Koester, L. Antonelli, S. Atzeni, F. Baffigi, D. Batani, C. Baird, N. Booth, and M. Galimberti *et al.*, High Power Laser Sci. Eng. **9**, e60 (2021).

[62] P. E. Masson-Laborde, M. C. Monteil, V. Tassin, F. Philippe, P. Gauthier, A. Casner, S. Depierreux, C. Neuville, B. Villette, S. Laffite *et al.*, Phys. Plasmas **23**, 022703 (2016).

[63] D. J. Strozzi, E. A. Williams, D. E. Hinkel, D. H. Froula, R. A. London, and D. A. Callahan, Phys. Plasmas **15**, 102703 (2008).

[64] S. Jorna, Phys. Fluids **17**, 765 (1974).

[65] C. L. Tang, J. Appl. Phys. **37**, 2945 (1966).

[66] V. Tikhonchuk, Y. J. Gu, O. Klimo, J. Limpouch, and S. Weber, Matter Radiat. Extremes **4**, 045402 (2019).

[67] D. H. Froula, J. S. Ross, L. Divol, N. Meezan, A. J. MacKinnon, R. Wallace, and S. H. Glenzer, Phys. Plasmas **13**, 052704 (2006).

[68] N. B. Meezan, R. L. Berger, L. Divol, D. H. Froula, D. E. Hinkel, O. S. Jones, R. A. London, J. D. Moody, M. M. Marinak, C. Niemann *et al.*, Phys. Plasmas **14**, 056304 (2007).

[69] L. Divol, R. L. Berger, N. B. Meezan, D. H. Froula, S. Dixit, P. Michel, R. London, D. Strozzi, J. Ross, E. A. Williams *et al.*, Phys. Plasmas **15**, 056313 (2008).

[70] V. T. Tikhonchuk, J. Fuchs, C. Labaune, S. Depierreux, S. Hüller, J. Myatt, and H. A. Baldis, Phys. Plasmas **8**, 1636 (2001).

[71] J. Fuchs, C. Labaune, S. Depierreux, V. T. Tikhonchuk, and H. A. Baldis, Phys. Plasmas **7**, 4659 (2000).

[72] M. Casanova, G. Laval, R. Pellat, and D. Pesme, Phys. Rev. Lett. **54**, 2230 (1985).

[73] R. L. Berger, S. Brunner, T. Chapman, L. Divol, C. H. Still, and E. J. Valeo, Phys. Plasmas **20**, 032107 (2013).

[74] P. M. Lushnikov and H. A. Rose, Plasma Phys. Controlled Fusion **48**, 1501 (2006).

[75] M. Grech, G. Riazuelo, D. Pesme, S. Weber, and V. T. Tikhonchuk, Phys. Rev. Lett. **102**, 155001 (2009).

[76] A. V. Maximov, I. G. Ourdev, D. Pesme, W. Rozmus, V. T. Tikhonchuk, and C. E. Capjack, Phys. Plasmas **8**, 1319 (2001).

[77] B. D. Fried and W. Gould, Phys. Fluids **4**, 139 (1961).